RSC Advances

PAPER

View Article Online
View Journal | View Issue

Cite this: *RSC Adv.*, 2024, **14**, 12829

Novel supramolecular luminescent metallogels containing Tb(III) and Eu(III) ions with benzene-1,3,5-tricarboxylic acid gelator: advancing semiconductor applications in microelectronic devices†

Subhendu Dhibar,‡*[a] Aiswarya Mohan,‡[b] Kripasindhu Karmakar, ‡[a] Bijnaneswar Mondal,[c] Arpita Roy,[d] Saranya Babu,[b] Parul Garg,[e] Pradip Ruidas,[f] Subham Bhattacharjee,[f] Sanjay Roy, [g] Ashok Bera, [e] Soumya Jyoti Ray, [d] Padmanabhan Predeep*[b] and Bidyut Saha *[a]

A novel strategy was employed to create supramolecular metallogels incorporating Tb(III) and Eu(III) ions using benzene-1,3,5-tricarboxylic acid (TA) as a gelator in *N*,*N*-dimethylformamide (DMF). Rheological analysis demonstrated their mechanical robustness under varying stress levels and angular frequencies. FESEM imaging revealed a flake-like hierarchical network for Tb–TA and a rod-shaped architecture for Eu–TA. EDX analysis confirmed essential chemical constituents within the metallogels. FT-IR, PXRD, Raman spectroscopy, and thermogravimetric analysis assessed their gelation process and material properties, showing semiconducting characteristics, validated by optical band-gap measurements. Metal–semiconductor junction-based devices integrating Al metal with Tb(III)- and Eu(III)-metallogels exhibited non-linear charge transport akin to a Schottky diode, indicating potential for advanced electronic device development. Direct utilization of benzene-1,3,5-tricarboxylic acid and Tb(III)/Eu(III) sources underscores their suitability as semiconducting materials for device fabrication. This study explores the versatile applications of Tb–TA and Eu–TA metallogels, offering insights for material science researchers.

Received 18th November 2023
Accepted 4th April 2024

DOI: 10.1039/d3ra07903a

rsc.li/rsc-advances

1. Introduction

Supramolecular gels represent a captivating class of materials formed through non-covalent interactions between molecules, driven by the intricate processes of self-assembly.[1,2] This phenomenon has brought about one of the most exciting outcomes of supramolecular self-assembly, continually expanding the frontiers of materials science and finding applications across a diverse spectrum. In the course of supramolecular gel formation, molecules within a solution coalesce into a robust three-dimensional network, effectively entrapping solvent molecules. This achievement is frequently confirmed through a straightforward inversion-vial test, illustrating the gel's successful development.[3] A variety of solvents, including water (H_2O),[4] acetonitrile ($H_3C–C{\equiv}N$),[5] ethanol (CH_3CH_2OH),[6] methanol (CH_3OH),[7] dichloromethane (CH_2Cl_2),[8] deuterated dichloromethane (CD_2Cl_2),[9] 1,2-dichlorobenzene ($C_6H_4Cl_2$),[10] acetone (CH_3COCH_3),[11] carbon tetrachloride (CCl_4),[12] DMF ($(CH_3)_2NC(O)H$),[13] tetrahydrofuran ($(CH_2)_4O$),[14] dimethyl sulfoxide (C_2H_6OS),[15] and toluene ($C_6H_5CH_3$),[16] are trapped within flexible gelators made of organic and/or inorganic components. These gelators form soft three-dimensional gel structures, accommodating a wide range of solvents used in the gel formation process.

Low molecular weight gelators (LMWGs) play a central role in the creation of supramolecular gels.[3,17] These gelators, through their ingenious design, initiate the self-assembly process in solutions, resulting in the formation of intricate gel-like structures. The distinctive allure of LMWG-based supramolecular gels lies in their ability to form complex

[a]*Colloid Chemistry Laboratory, Department of Chemistry, The University of Burdwan, Golapbag, Burdwan 713104, West Bengal, India. E-mail: sdhibar@scholar.buruniv.ac.in; bsaha@chem.buruniv.ac.in; Tel: +91 7001575909; +91 9476341691*

[b]*Laboratory for Molecular Photonics and Electronics (LAMP), Department of Physics, National Institute of Technology Calicut, Calicut 673603, Kerala, India. E-mail: predeep@nitc.ac.in*

[c]*Department of Chemistry, Guru Ghasidas Vishwavidyalaya, Bilaspur 495009, Chhattisgarh, India*

[d]*Department of Physics, Indian Institute of Technology Patna, Bihar 801106, India*

[e]*Department of Physics, Indian Institute of Technology Jammu, J&K 181221, India*

[f]*Department of Chemistry, Kazi Nazrul University, Asansol 713303, West Bengal, India*

[g]*Department of Chemistry, School of Science, Netaji Subhas Open University, Kalyani Regional Centre, Kolkata 741251, India*

† Electronic supplementary information (ESI) available. See DOI: https://doi.org/10.1039/d3ra07903a

‡ SD, AM and KK should be treated as joint first authors.

three-dimensional networks orchestrated by non-covalent interactions like hydrogen bonds,[18] electrostatic interactions,[19] hydrophobic,[20] and hydrophilic forces,[21] van der Waals forces,[18] aryl-system-based interactions,[22] *etc.* These interactions confer upon them exceptional properties and multifaceted applications. The concept of employing LMWGs in supramolecular gelation brings with it a host of benefits. The deliberate manipulation of their molecular structures allows for meticulous tailoring of key attributes such as gel strength, responsiveness to external stimuli, and their capacity for encapsulation. By adeptly designing the chemical composition of LMWGs, researchers can modulate the specific interactions dictating gel formation, leading to materials with bespoke functionalities. The realm of applications for LMWG-based supramolecular gels is strikingly extensive. Supramolecular gels exhibit a wide array of potential applications that span various domains. These applications encompass areas like optoelectronic devices,[23] where their utility has been explored for enhanced light-emitting capabilities, chemosensors that enable the detection of specific molecules,[24] and catalysis for promoting chemical reactions.[4a,b] Additionally, their adaptability extends to medical diagnostics,[25] lithography techniques for pattern formation,[26] and the development of efficient electrochemical devices.[27] Supramolecular gels have also found utility in cell culturing practices,[28] enabling enhanced conditions for cell growth, as well as in drug delivery strategies to ensure controlled release.[29] Furthermore, their role extends to facilitating biomineralization processes,[30] supporting tissue engineering endeavors,[31] contributing to advancements in biochemistry,[32] and aiding in the removal of pollutants from various environments.[33] The versatility of supramolecular gels thus holds promise across a rich spectrum of applications, embodying their potential to address a multitude of challenges and needs.

Metallogels form when metal ions interact with specific molecules, often low molecular weight gelators. This interaction creates a gel-like structure with unique properties, influenced by metal ion coordination and self-assembly. Metallogels differ from traditional gels by incorporating metal ions, offering diverse functional characteristics. Formation involves metal ion and gelator self-assembly *via* coordination bonds, resulting in a solvent-trapped network. This network can be reversible, enabling the metallogel to respond to changes in external conditions. Metallogels have garnered significant interest due to their potential applications in various fields such as redox activity,[34] magnetic behavior,[35] conductivity,[36] actuation,[37] catalytic activity,[4a,b] and optical properties.[38]

Compared to metallogels with 3d transition metals, those featuring lanthanides showcase even more intriguing traits. Lanthanide metallogels form *via* coordination-driven self-assembly, incorporating lanthanide ions. Their distinct properties stem from complex interactions, making them versatile across various applications. These applications span diverse fields, including their utilization in light-emitting devices,[39] optical materials,[40] forensic science applications,[41] drug delivery systems,[42] bioimaging techniques,[43] chemical and biosensing technologies,[44] solar cell devices,[45] artificial photosynthesis endeavors,[46] phase-separation absorption,[47] solid-state lighting and stimuli-responsive,[48] *etc.* The wide-ranging capabilities of these lanthanide-ion-based supramolecular metallogels make them integral components in driving innovation across multiple disciplines.

Various studies have documented lanthanide-ion-based metallogels, such as Holten-Andersen's multistimuli-responsive metallogels emitting white light[49] and Alves Jr's luminescent hydrogels.[50] Maitra *et al.* showcased facile formation of metallogels with lanthanide(III) cholates.[51] Inspired by these, we synthesized metallogels anchored in terbium(III) and europium(III) ions using low-molecular-weight organic constituents. Employing benzene-1,3,5-tricarboxylic acid, gelation occurred in *N*,*N*-dimethylformamide under ordinary conditions, laying groundwork for customizable electronic devices. Tb–TA and Eu–TA metallogels displayed resilience against gravitational forces, affirmed by the inversion vial test. Our investigation included evaluating mechanical properties and morphological characteristics. With the aim of developing metallogel-facilitated metal–semiconductor junction devices, we successfully constructed a Schottky barrier diode.

2. Experimental

2.1. Materials

Terbium(III) acetate hydrate (99.9% trace metals basis), europium(III) acetate hydrate (99.9% trace metals basis) benzene-1,3,5-tricarboxylic acid (95%) were purchased from Sigma-Aldrich chemical company and used as received. Dry solvent (*i.e.* *N*,*N*-dimethyl formamide (DMF)) was used for entire work.

2.2. Apparatus and measurements

The mechanical study employed a rheometer manufactured by TA Instruments.

Microstructure data was obtained using a Carl Zeiss SUPRA 55VP field-emission scanning electron microscope (FESEM). The energy-dispersive X-ray spectroscopy (EDX) analyses were carried out with a Bruker Super detector.

Fourier transform infrared spectra obtained through a JASCO FTIR 4700 spectrometer.

A PANALYTICAL X'pert powder X-ray diffractometer with Cu Kα1 radiation is employed to obtain the nature of the metallogels.

Raman analysis of metallogels are carried out using a HORIBA LABRAM HR evolution confocal Raman spectrometer with an excitation source of 532 nm (100 mW).

TGA is carried out at a heating rate of 10 °C min^{-1} under nitrogen atmosphere using Hitachi STA7200 analyzer.

To obtain the current–voltage (*I*–*V*) characteristics of our synthesized metallogel material-based thin film device, we utilized a Keithley 2612A Sourcemeter interfaced with a computer.

2.3. Synthesis of terbium(III)- and europium(III)-metallogel

Terbium(III) acetate hydrate (99.9% trace metals basis, 0.336 g, 1 mmol) was dissolved in *N*,*N*-dimethylformamide solvent (500

μL) within a glass vial at room temperature, resulting in a colorless solution. Similarly, benzene-1,3,5-tricarboxylic acid (95%, 0.210 g, 1 mmol) was dissolved in DMF (500 μL), yielding a colorless solution of benzene-1,3,5-tricarboxylic acid in DMF. Combining the colorless DMF solution of benzene-1,3,5-tricarboxylic acid with the Tb(III)-salt solution resulted in the emergence of a dense white mixture. This mixture was subjected to sonication for approximately 10 minutes under ambient conditions. The outcome was the creation of a white-colored metallogel featuring Tb(III) ions, referred to as Tb–TA. This gel formation was stabilized within an open atmosphere, as illustrated in Fig. 1. The Tb–TA metallogel exhibited a striking fluorescent green glow when exposed to UV light at 366 nm within a UV-light chamber (Fig. 1). Impressively, the Tb–TA metallogel maintained its stability for a minimum of six months. Notably, the successful inversion vial test presented in Fig. 1 offers conclusive evidence of the Tb–TA metallogel's stability and integrity.

By employing the identical synthetic procedure, a europium(III)-metallogel was synthesized. This process involved combining 500 μL of a *N*,*N*-dimethylformamide solution containing europium(III) acetate hydrate (99.9% trace metals basis, 0.329 g, 1 mmol) and benzene-1,3,5-tricarboxylic acid (95%, 0.210 g, 1 mmol) in a glass vial at room temperature. The resulting mixture was sonicated for around 10 minutes under normal conditions. The outcome was the development of a metallogel with a white hue that incorporated Eu(III) ions, termed as Eu–TA. Importantly, this gel formation process occurred in an open environment, as demonstrated in Fig. 1. When exposed to UV light at 366 nm in a UV-light chamber (as depicted in Fig. 1), the Eu–TA metallogel emitted a remarkable fluorescent red glow. Impressively, the Eu–TA metallogel retained its structural integrity for a minimum of six months. It is noteworthy that the conclusive evidence of the stability and integrity of the Eu–TA metallogel is provided by the successful inversion vial test, as shown in Fig. 1.

The concentrations of $Tb(CH_3COO)_3 \cdot H_2O$ and benzene-1,3,5-tricarboxylic acid were systematically varied within a defined range (30–546 mg mL^{-1}) to assess the Minimum Gelation Concentration (MGC) of the Tb–TA metallogel. In this investigation, the ratio between the components responsible for forming the Tb–TA metallogel was consistently maintained at $[Tb(CH_3COO)_3 \cdot H_2O]$: [benzene-1,3,5-tricarboxylic acid] = 1 : 1 (w/w). The Tb–TA metallogel exhibiting a stable white appearance was successfully obtained at a concentration of 546 mg mL^{-1} of Tb(III)-acetate salt and benzene-1,3,5-tricarboxylic acid in the solvent DMF. Similarly, to determine the MGC of the Eu–TA metallogel, the concentrations of $Eu(CH_3COO)_3 \cdot H_2O$ salt and benzene-1,3,5-tricarboxylic acid were systematically adjusted across a range of 30–539 mg mL^{-1}. A well-formed and stable Eu–TA metallogel was achieved at a concentration of 539 mg mL^{-1} of Eu(III)-acetate salt and benzene-1,3,5-tricarboxylic acid in the DMF solvent.

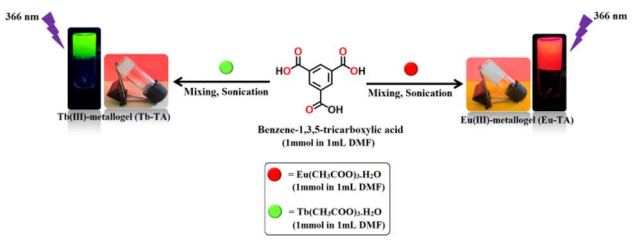

Fig. 1 Synthetic route of Tb(III)-metallogel (Tb–TA) and Eu(III)-metallogel (Eu–TA) and their inverted photography images showing the stability of gel materials.

3. Results and discussion

3.1. Rheological analysis

Rheological investigations were carried out to validate the viscoelastic semisolid properties of both the Tb(III)-metallogel and Eu(III)-metallogel. The confirmation of material viscoelasticity relies on the storage modulus (G') exceeding the loss modulus (G''). These moduli were measured to characterize the gel's behavior. Within the viscoelastic range, the system conserves energy as represented by G', analogous to $(\sigma_0/\gamma_0)\cos(\delta)$, while simultaneously dissipating energy due to oscillatory stress, represented by G'', resembling $(\sigma_0/\gamma_0)\sin(\delta)$. For classification as a gel, the condition $G'(\omega) > G''(\omega)$ must be met, where $G'(\omega)$ is approximately equal to ω° and ω denotes the angular frequency. In the specific case of the Tb(III)-metallohydrogel, with a consistent $Tb(CH_3COO)_3 \cdot H_2O$ concentration ([Tb(III)] = 546 mg mL^{-1}), experimental rheology results indicated a significantly higher storage modulus (G') compared to the loss modulus (G'') ($G' \gg G''$) (Fig. 2a). This rheological data unequivocally confirms that the Tb(III)-metallogel retains its gel-like structural characteristics and demonstrates behavior of semi-solid like. In Fig. 2b, the strain-sweep experiment

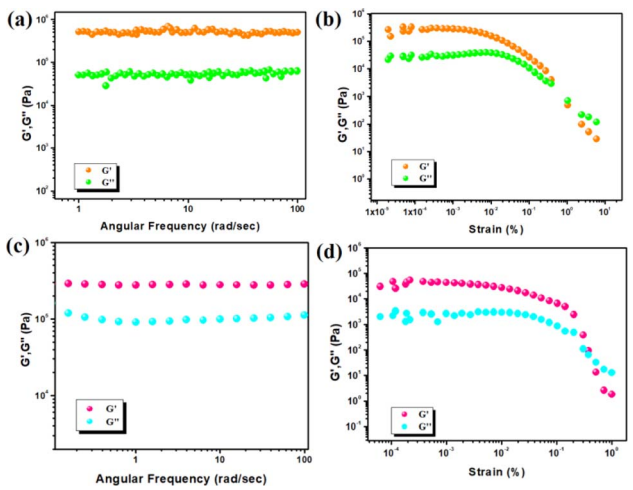

Fig. 2 (a) The graph presents the correlation between angular frequency and the storage modulus (G') as well as the loss modulus (G'') of the Tb–TA metallogel; (b) strain-sweep tests were carried out on the Tb–TA metallogel, maintaining a steady frequency of 6.27997 rad s^{-1}; (c) angular frequency measurements are plotted against the values of G' and G'' for the Eu–TA metallogel; (d) strain-sweep measurements of the Eu–TA metallogel were executed, maintaining a consistent frequency of 6.283 rad s^{-1}.

conducted on the Tb(III)-metallogel material maintains a constant frequency of 6.27997 rad s^{-1}. The constant frequency of 6.27997 rad s^{-1} ensures that the experiment focuses on the effect of strain amplitude variation while keeping the deformation frequency consistent, allowing for a more controlled analysis of the gel's rheological behavior.

The Eu–TA metallogel have a gel nature and exhibits semi-solid-like behaviour since $G' > G''$. For the europium(III)-metallogel, specifically focusing on a consistent concentration of $Eu(CH_3COO)_3 \cdot H_2O$ ([Eu(III)] = 539 mg mL^{-1}), the results of experimental rheology revealed a notably elevated storage modulus (G') in comparison to the loss modulus (G'') ($G' \gg G''$) (Fig. 2c). These rheological findings provide unequivocal evidence that the Eu–TA metallogel preserves its gel-like structural attributes and exhibits behavior analogous to that of a solid. In Fig. 2d, a strain-sweep experiment is depicted, focusing on the Eu–TA metallogel material, with a constant frequency of 6.283 rad s^{-1}. The maintenance of a constant frequency of 6.283 rad s^{-1} ensures that the experimental conditions remain consistent, allowing for a controlled analysis of the gel's rheological behavior with respect to changes in strain amplitude.

3.2. Investigation of the microstructure of Tb–TA and Eu–TA metallogels

The structural analysis of both the Tb–TA and Eu–TA metallogels was conducted using FESEM (Field Emission Scanning Electron Microscopy) analysis to explore their respective microstructural patterns. For the Tb–TA metallogel, FESEM images unveiled a hierarchical architecture resembling flake-like structures (Fig. 3a–d). These distinctive hierarchical morphologies, observed within the FESEM analysis, are postulated to originate from the combination of $Tb(OAc)_3 \cdot H_2O$ and benzene-1,3,5-tricarboxylic acid gelator in DMF solvent. This synthesis process is facilitated by rapid mixing and various non-covalent interactions. The confirmation of this composition came from EDX (Energy Dispersive X-ray) elemental mapping and spectra, confirming the presence of carbon (C), nitrogen (N), oxygen (O), and terbium (Tb) elements. These elements correspond to the $Tb(OAc)_3 \cdot H_2O$ and benzene-1,3,5-tricarboxylic acid gelator, as well as the DMF solvent. These components collectively contribute to the network formation within the $Tb(OAc)_3 \cdot H_2O$ metallogel (Fig. 3e–i) (please see Fig. S1 for EDX spectra of Tb–TA metallogel in ESI†).

In comparison, the microstructural analysis of the Eu–TA metallogel was also performed using FESEM analysis, revealing a distinct hierarchical architecture resembling rod-like structures (Fig. 4a–d). Similar to the Tb–TA case, these hierarchical morphologies observed within the FESEM analysis are believed to arise from the combination of $Eu(OAc)_3 \cdot H_2O$ and benzene-1,3,5-tricarboxylic acid gelator in DMF solvent, facilitated by rapid mixing and non-covalent interactions. To validate the composition of the Eu–TA metallogel, EDX elemental mapping and spectral analysis were employed, confirming the presence of carbon (C), nitrogen (N), oxygen (O), and europium (Eu) elements. These elements correspond to the $Eu(OAc)_3 \cdot H_2O$ and benzene-1,3,5-tricarboxylic acid gelator, along with the DMF solvent. This combination of constituents contributes to the network formation within the Eu–TA metallogel (Fig. 4e–i) (please see Fig. S2 for EDX spectra of Eu–TA metallogel in ESI†).

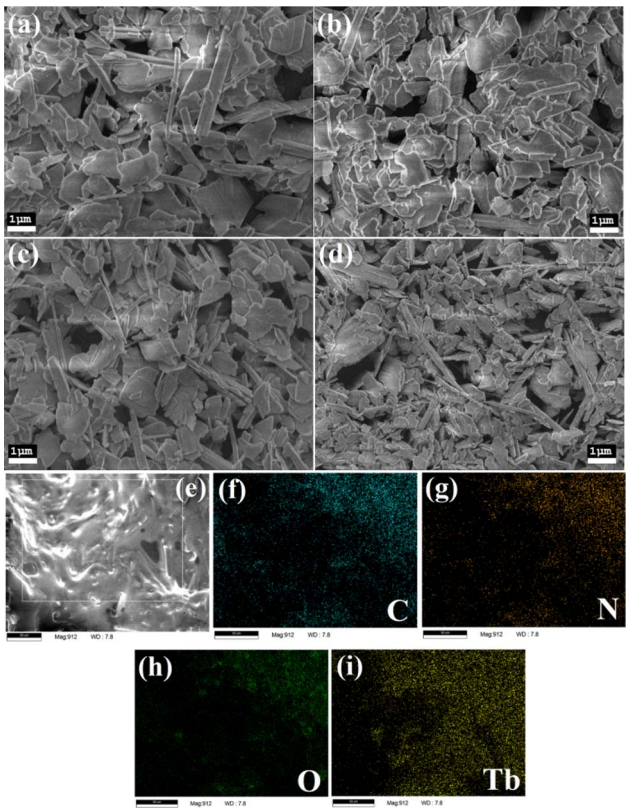

Fig. 3 (a–d) Microstructural patterns of the Tb–TA metallogel captured through Field Emission Scanning Electron Microscopy (FESEM) images; (e–i) spatial distribution of crucial elements, encompassing carbon (C), nitrogen (N), oxygen (O), and terbium (Tb), revealed through elemental mapping.

In summary, both the Tb–TA and Eu–TA metallogels exhibit intriguing hierarchical architectures under FESEM analysis, indicating their unique structural characteristics originating from specific combinations of components and interactions during their synthesis processes.

3.3. Fourier transform infrared (FTIR), powder X-ray diffraction (PXRD), Raman spectroscopy and thermogravimetric analysis (TGA) of Tb–TA and Eu–TA metallogel

The confirmation of acetate and carboxylic groups associated with $Eu(OAc)_3 \cdot H_2O$, $Tb(OAc)_3 \cdot H_2O$, and benzene-1,3,5-tricarboxylic acid was established through FTIR spectra analysis performed using a JASCO FTIR 4700 spectrometer. The FTIR spectra of Tb–TA metallogel, Eu–TA metallogel, $Tb(OAc)_3 \cdot H_2O$, $Eu(OAc)_3 \cdot H_2O$, and benzene-1,3,5-tricarboxylic acid are illustrated in Fig. 5a and b.

In the Tb–TA metallogel, the presence of $Tb(OAc)_3 \cdot H_2O$ and benzene-1,3,5-tricarboxylic acid is discerned by the appearance of narrow and sharp peaks, particularly evident in the region

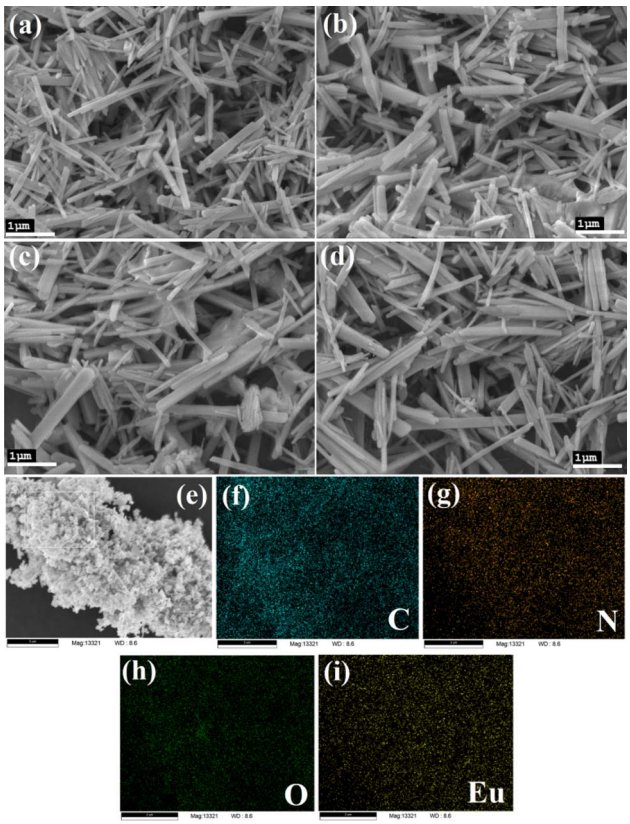

Fig. 4 (a–d) Microstructural analysis of the Eu–TA metallogel depicted through Field Emission Scanning Electron Microscopy (FESEM) images. (e–i) Elemental mapping revealing the spatial distribution of essential components, encompassing carbon (C), nitrogen (N), oxygen (O), and europium (Eu).

between 500 cm^{-1} and 680 cm^{-1} (Fig. 5a).[52] This spectral region is indicative of the interaction between benzene-1,3,5-tricarboxylic acid and $Tb(OAc)_3 \cdot H_2O$. The wave numbers within the 2800–3000 cm^{-1} range signify the presence of $-CH_3$, $-CH_2$, and –CH stretch vibrations.[53] Peaks around 3272 cm^{-1} and 1032 cm^{-1} signify –OH stretch vibrations, while sharp peaks at 1441.5 cm^{-1} and 1537.9 cm^{-1}, along with a broad peak at 2500–3200 cm^{-1}, signify the formation of carboxylic acid.[53] The range 3300–3500 cm^{-1} corresponds to the broad stretching of H_2O vibration absorption. Peaks around 555 cm^{-1} and 920 cm^{-1} correspond to the out-of-plane vibration of crystalline water molecules and in-plane swing vibration of coordinated water molecules, respectively, confirming the existence of both types of water molecules within the gel composition.[52,54]

In the case of the Eu–TA metallogel, IR peaks at 671.1 cm^{-1}, 938.1 cm^{-1}, 1536.9 cm^{-1}, and 3281.2 cm^{-1} indicate the presence of $Eu(OAc)_3 \cdot H_2O$ in the synthesized gel (Fig. 5b).[55] Similarly, benzene-1,3,5-tricarboxylic acid's presence is reflected by various IR peaks, such as 526.4 cm^{-1}, 1105.9 cm^{-1}, and 3001.6 cm^{-1}.[56] The carbonyl and hydroxyl groups are crucial in characterizing carboxylic acid derivatives. The presence of the carbonyl group is a significant feature in the infrared spectrum due to its high sensitivity to environmental changes and strong absorption intensity. The various effects, such as inductive,

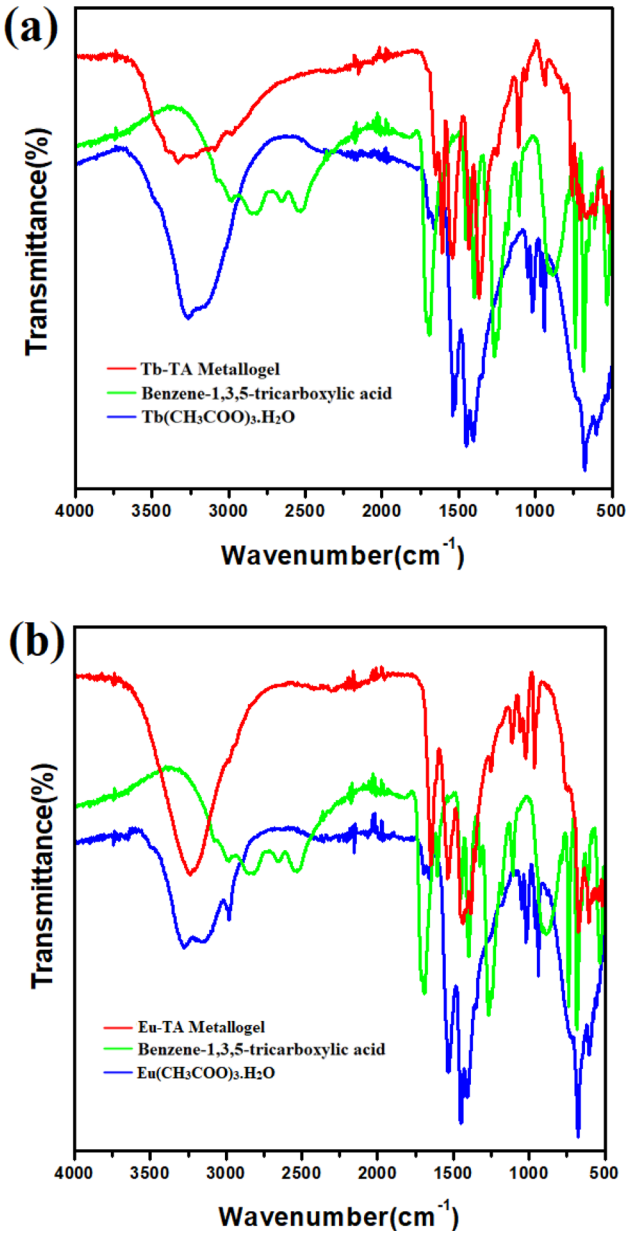

Fig. 5 (a) Comparative FTIR spectra for the xerogel variant of Tb–TA metallogel, benzene-1,3,5-tricarboxylic acid, and terbium(III) acetate hydrate; (b) comparative FTIR spectra for the xerogel variant of Eu–TA metallogel, benzene-1,3,5-tricarboxylic acid, and europium(III) acetate hydrate.

mesomeric, field, and conjugation effects, lead to intra- and inter-molecular hydrogen bonding, which impacts carbonyl and absorption patterns in organic compounds. Bands observed at 1368.2 cm^{-1} and 1432.8 cm^{-1} are assigned to C–O stretching, while 1608.3 cm^{-1} corresponds to C=O stretching.[56] The broad band between 3400 cm^{-1} and 3600 cm^{-1} indicates O–H stretching vibrations, particularly attributed to the O–H stretching of the carboxylic acid group. The region at 1705 cm^{-1} is assigned to vibrations of acetate groups.[55] FTIR spectra analysis offers a comprehensive understanding of the presence of specific functional groups and interactions within the Tb–TA

(Fig. 5a) and Eu–TA (Fig. 5b) metallogels, shedding light on their distinct compositions and structural properties.

Carboxylic acids as ligands form binuclear compounds, in which an indirect interaction[56] between the metal centers takes place. In this work, trimesic acid is capable of coordinating with europium(III) and terbium(III) of europium acetate and terbium acetate respectively. The aromatic ring in trimesic acid facilitates carboxylic groups (COOH) capable of chelating cations and charge transfer to the metal ions. The FTIR spectrum of Eu–TA metallogel and Tb–TA metallogel shows a shift of the carbonyl bond frequencies. The symmetric and asymmetric variations in the frequencies[56] of the COO–Eu and Tb bond-stretching band for Eu–TA and Tb–TA (between 1406 cm^{-1} and 1538 cm^{-1}) were lower. This reflects the coordination of trimesic acid with europium acetate and terbium acetate. The new peaks in Eu–TA metallogel at 1608 and 1705 cm^{-1} correspond to the asymmetric stretching vibration[57] of COO–. This indicates the coordination between lanthanide ions and trimesic acid.

The crystalline nature of the metallogels was investigated using a PANalytical X'pert powder X-ray diffractometer equipped with Cu $K_{\alpha 1}$ radiation. The powder X-ray diffraction (PXRD) patterns for Tb–TA and Eu–TA metallogels are illustrated in Fig. 6. Further PXRD patterns for $Tb(OAc)_3 \cdot H_2O$, $Eu(OAc)_3 \cdot H_2O$, and benzene-1,3,5-tricarboxylic acid are provided in the ESI as Fig. S3–S5,† respectively.

For the Tb–TA metallogel, the presence of crystallinity is evident from Fig. 6, which displays distinctive 2θ values at 9.79°, 11.5°, 18.9°, 21.8°, 25.4°, and 27.4°. These peaks are likely attributed to $Tb(OAc)_3 \cdot H_2O$ (Fig. S3†). At room temperature, the XRD profile of the Eu–TA metallogel (Fig. 6) reveals the coexistence of $Eu(OAc)_3 \cdot H_2O$ and benzene-1,3,5-tricarboxylic acid, as indicated by the 2θ values at 11.7°, 19.2°, 21.4°, and 25.1° (associated with $Eu(OAc)_3 \cdot H_2O$, Fig. S4†), as well as at 10.5°, 20.2°, 24.5°, 27.3°, and 33.3° (attributed to benzene-1,3,5-tricarboxylic acid, Fig. S5†). Particularly noteworthy is the pronounced peak at 10.5°, which can be attributed to benzene-1,3,5-tricarboxylic acid. The additional 2θ values, including 10.23°, 12.3°, 14.2°, 20.2°, 23.8°, 24.8°, 26.8°, 27.4°, 30.4°, 33.08°, and 42.7°, stem from the presence of benzene-1,3,5-tricarboxylic acid within the gel matrix (Fig. S5†). Conversely, the PXRD pattern of the Tb–TA metallogel showcases a comparatively higher count of distinct sharp peaks with elevated intensities compared to the Eu–TA metallogel. This distinction indicates a more robust crystalline nature for the Tb–TA metallogel.

Structural characteristics of the gels are further explored using Raman studies. Raman analysis of both Tb–TA and Eu–TA metallogels are carried out using a HORIBA LABRAM HR evolution confocal Raman spectrometer with an excitation source of 532 nm (100 mW). Fig. 7a and b show the Raman spectrum of Tb–TA and Eu–TA metallogels respectively. Benzene-1,3,5-tricarboxylic acid is the common component used here for the formation of both the metallogels. Naturally its signatures in the form of C–H vibrations, carboxylic acid group vibrations and ring vibrations are clearly visible in both the Raman spectra. The Raman shift in the range 3000–3100 cm^{-1} is an identification of C–H stretching vibrations which points to the presence of a hetero-aromatic organic molecule.[58] This is conspicuous by its absence in case of Eu–TA metallogel (Fig. 7b), while the band at 3011.5 cm^{-1} shows the

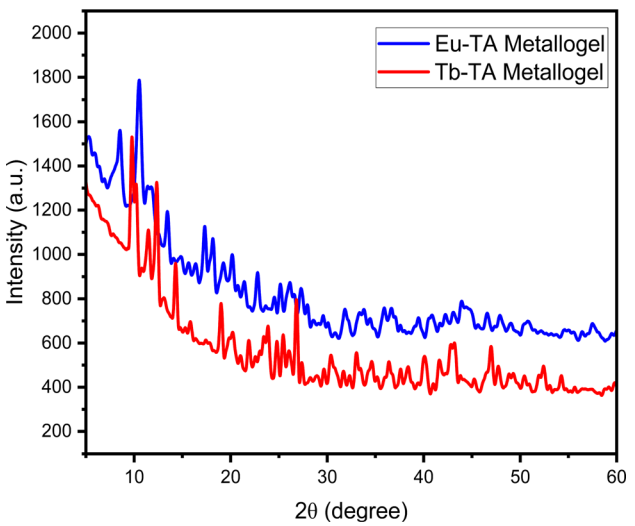

Fig. 6 The PXRD pattern of Tb–TA xerogel and Eu–TA xerogel demonstrating its crystalline nature.

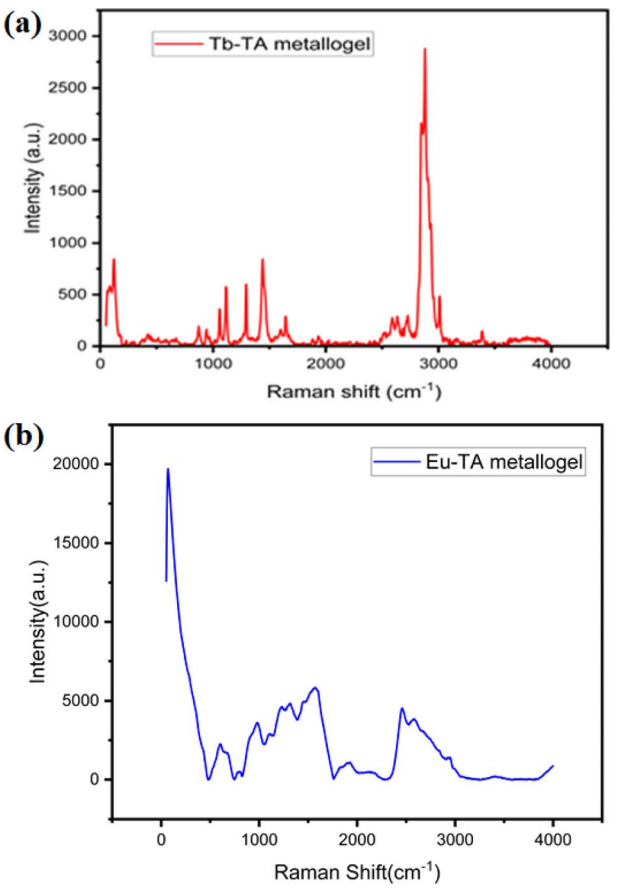

Fig. 7 (a) Raman spectrum of Tb–TA metallogel; (b) Raman spectrum of Eu–TA metallogel.

C–H stretching vibrations in Tb–TA metallogel (Fig. 7a). The range 750–1300 cm^{-1} corresponds to the C–H in-plane and out-of-plane bending vibrations in aromatic compounds.[58] O–H stretching of carboxylic acid group of trimesic acid is clearly indicated by a broad band appearing in the region 3400–3600 cm^{-1}.[58] The various impure modes that receive contributions from other modes can be observed below 1000 cm^{-1} in both metallogels.[58] This is most probably due to the in-plane and out-of-plane vibration of the benzene ring. Moreover, the fluorescence lifetime of both the metallogels measured by fitting the curves with exponential decay profiles (Fig. S8†). For both the metallogels, excitation wavelength was 340 nm and emission was monitored at 480 nm. In this regard, the observed lifetime of Eu–TA metallogel was 1.28 ns whereas Tb–TA metallogel showed 1.56 ns (Fig. S6 and S7†).

Thermogravimetric analysis (TGA) is used to investigate the thermal stability of the gels. TGA is carried out at a heating rate of 10 °C min^{-1} under nitrogen atmosphere using Hitachi STA7200 analyzer. Fig. 8 shows the gravimetric thermogram of the gels. In both the metallogels, the early weight losses at around 100 to 200 °C follow almost a similar pattern and these losses may be, most probably, due to the loss of the moisture content. After that Eu–TA degrades fast in two major steps while Tb–TA maintains an almost monotonous path till around 400 °C before finally rushing to calcination. The calcination occurs approximately at 440 °C for Tb–TA metallogel and at 663 °C for Eu–TA metallogel respectively, leading to a black coloured material.[59] It has been shown that the decomposition of acetate starts near 145 °C and terminates at around 663 °C.[53] However, the initial degradation temperature of benzene-1,3,5-tricarboxylic acid starts at 300 °C and continue up to 500 °C where a sharp degradation results.[59] It is clear that the difference in the observed behaviour of the Tb–TA and Eu–TA metallogels is due to the characteristic differences in the terbium and europium metal acetates present in their respective combinations. The TGA studies thus show clear and discernible thermal behaviour with the Tb–TA metallogel exhibiting better thermal stability.

3.4. Device fabrication of Tb–TA and Eu–TA metallogels

An exploration into the semiconductor characteristics of Tb–TA and Eu–TA metallogels has been initiated, aiming to uncover their potential applications in electronic devices. The intriguing possibilities encompass utilizing them as charge transport buffer layers, components for Schottky diodes, or elements in thin film transistors. Nonetheless, for these applications to materialize effectively, it is imperative that these materials can form uniform and nanoscale-thick films without the presence of pinholes. This task is complicated by the inherent gel-like nature of these materials, which often hampers the creation of such thin films. To circumvent this challenge, a viable approach was adopted by combining the gels with an insulating polymer, polymethylmethacrylate (PMMA). A pivotal observation was made that with a meticulous and optimized stirring process, well-dispersed blends of these gels and PMMA could be achieved in the solvent DMF. Significantly, DMF was found to serve as a suitable solvent for both the gels and PMMA. The procedure involved stirring PMMA in DMF at 40 °C for duration of two hours, followed by the addition of the gels. Subsequent stirring for an additional four hours led to the formation of finely dispersed blends. To ascertain the ideal PMMA-to-gel ratio, different weight percentages of PMMA (ranging from 10% to 50%) were mixed with the gels, and the film-forming capabilities of each composition were scrutinized. Moreover, the electrical properties of these compositions were assessed. The results unveiled that the most optimal film properties were exhibited by the blend composition comprising an equal proportion of the gel and PMMA. This finding highlights the potential of such hybrid compositions for overcoming the film-forming challenges posed by the gel nature of these materials. The semiconducting electrical and charge transport characteristics of both gels were assessed by fabricating Schottky device structures employing blend films of gel and PMMA as the active semiconducting layer. These films were sandwiched between a transparent conducting electrode made from Indium Tin Oxide (ITO) serving as the anode, and aluminium (Al) acting as the cathode. The schematic representation of the utilized device structure is illustrated in Fig. 9. The ITO substrates, obtained from Ossila (UK), were pre-patterned and underwent a cleaning

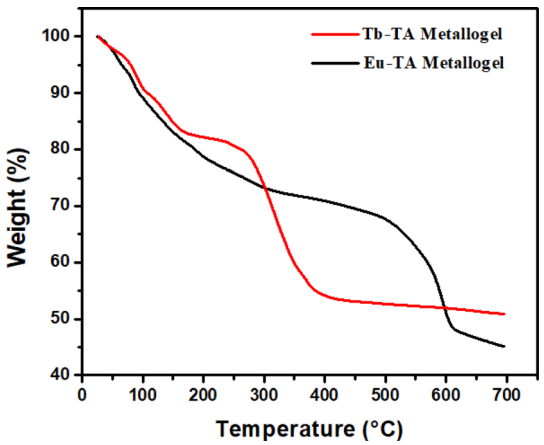

Fig. 8 Thermogravimetric analysis of Tb–TA (red) and Eu–TA metallogel (black).

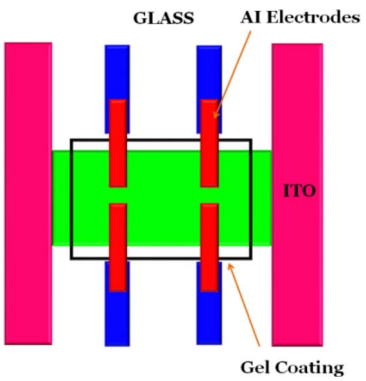

Fig. 9 Schematic sketch of the device structure for the gels Tb–TA and Eu–TA metallogels.

process involving soap solution, followed by sonication in highly pure deionized water. Subsequently, isopropyl alcohol sonication and a 12 minute UV/ozone exposure ensured thorough cleaning. The gel composite films were then spin-coated onto these ITO substrates at a speed of 1500 rpm, resulting in film thicknesses around 200 nm. These coated films were immediately annealed at 60 °C for 5 minutes. Through thermal deposition under high vacuum conditions (10^{-5} torr) and utilizing a precisely fitting metal mask, aluminium (Al) electrodes were deposited onto the active layer. The final device structure consisted of ITO/Tb–TA (or Eu–TA) gel-PMMA blend/Al. Employing a custom-made device holder featuring spring-loaded gold contacts, the current–voltage (I–V) characteristics of all devices were assessed. This analysis was conducted using a Keithley 2612A source meter interfaced with a computer, allowing for a comprehensive understanding of the device's performance.

3.5. Electrical characterization

The current–voltage (I–V) characteristics of the Tb–TA and Eu–TA metallogel Schottky devices are shown in the Fig. 10. It can be seen that both I–V characteristics are wide and nonlinear. This wide nature of the curves usually derives from high series resistance of the device.[60] For evaluating the device operating parameters which can help to throw some light in the possible semiconducting properties of the gels, we used the usual thermionic emission theory based on the Cheung's method.[61] The diode equation is accordingly given as,

$$I = I_0\left(\frac{qV}{\eta KT}\right)\left[1 - \exp\left(\frac{-qV}{\eta KT}\right)\right] \quad (1)$$

where V is the applied bias voltage, k the Boltzmann constant, q the electronic charge, T the temperature and I_0 represents the usual reverse saturation current. Accordingly,[61]

$$I_0 = AA^*T^2 \exp\left(\frac{-q\varphi_B}{\eta KT}\right) \quad (2)$$

$$\frac{dV}{d\ln I} = \left(\frac{\eta KT}{q}\right) + IR_s \quad (3)$$

$$H(I) = V - \left(\frac{\eta KT}{q}\right)\ln\left(\frac{I}{AA^*T^2}\right) \quad (4)$$

$$H(I) = IR_s + \eta\varphi_B \quad (5)$$

Here (R_s) is the series resistance, (η) is the ideality factor, and (φ_B) is the barrier potential height (φ_B). $H(I)$ is a function defined for evaluating the diode parameters. The ideality factor is obtained by fitting the plot between $\frac{dV}{d(\ln I)}$ and I. This plot also will give the series resistance, R_s. H *vs.* I plot is also used as another method to calculate R_s as well as to arrive at the barrier height, (φ_B). Fig. 11 and 12 respectively show all these plots for Tb–TA and Eu–TA metallogel blends.

At low bias voltage, the I–V characteristics of the Schottky diode is linear. It is different in case of higher voltage. The effect of series resistance[62] and interface state density will deviate the I–V characteristics from linearity. Double log plots of I and V are used to establish the charge transport behaviour and mechanisms at the interface of the gel semiconductor and electrodes.

Variations in the slopes of these curves give indication about the type of mechanism of charge transport. Fig. 13a and

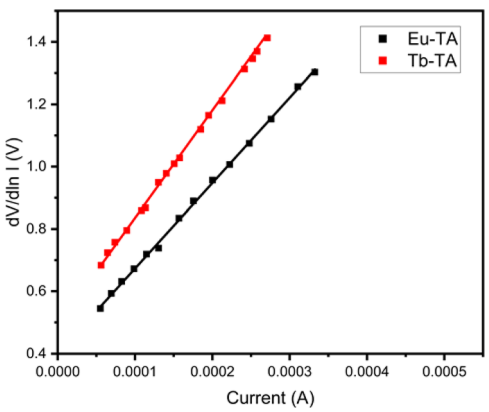

Fig. 11 $\frac{dV}{d(\ln I)}$ *vs.* I plots of Tb–TA metallogel and Eu–TA metallogel based Schottky diodes.

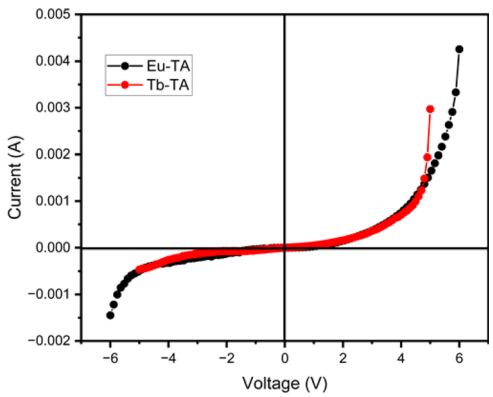

Fig. 10 I–V characteristics of Tb–TA and Eu–TA metallogel based diodes.

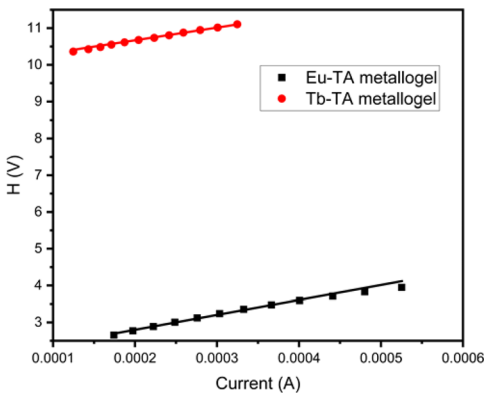

Fig. 12 H *vs.* I plots of Tb–TA and Eu–TA metallogel based Schottky diodes.

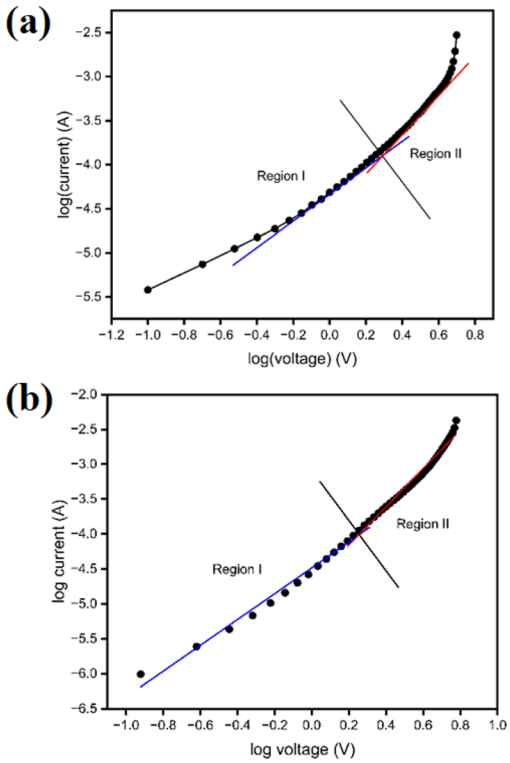

Fig. 13 (a and b) Log I *vs.* log V plots of Tb–TA and Eu–TA metallogel based Schottky diodes.

b represents the log–log plots for Tb–TA and Eu–TA metallogels respectively. Two regions I and II are indicated in the figure. These regions show different slopes with $I \propto V^m$, where m is the slope of the plot for each linear region. The current conduction mechanism at the low bias region I exhibits an ohmic behavior $I \propto V$. This is due to the thermally generated carriers. In high voltage region II, the linearity gives away to $I \propto V^2$, where the current is Space Charge Limited (SCLC regime) and trap free. Here one can use the Mott–Gurney equation[63]

$$I = \frac{9}{8}\varepsilon_r\varepsilon_0\mu A\frac{V^2}{d^3} \quad (6)$$

Here ε_0 the permittivity of free space, ε_r the dielectric constant of the blend, μ is the charge carrier mobility, and d is the thickness of the film. By fitting the SCLC region II of log I–log V plot (Fig. 13) the electron mobility is extracted. Thus we can conclude that the thermally generated carriers are dominant at low voltage region[64] and thus the injected carriers from the contacts are neutralized by the thermally generated carriers. Therefore the domination of Ohm's law is clearly visible in the low voltage region. The space charge limited conduction mechanism begins[64] when the density of the injected carriers from the contacts becomes comparable with the density of the thermally generated free carriers. The applied voltage in which this transition occurs is called the critical voltage. Thus the transition point in the log(I)–log(V) behavior, from the linear state to region II ($I \propto V^2$), is determined by the point where the slope of the curve changes from 1 to 2. The estimated values of series resistance, ideality factor, barrier potential, conductivity ON/OFF ratio, and electron mobility for both the Schottky device made with Tb–TA and Eu–TA metallogel blends are presented in Table 1.

The conductivity values of both the gel devices are high enough to be categorized them as materials with high semiconducting electric properties. However the series resistances of the diodes are too high for a good Schottky device. Another interesting parameter that shows too high values is the ideality factor. Such high values of ideality factor are reported earlier too for Schottky diodes. In simple terms this parameter is an indication of the variation of the diode slopes from a typical ideal diode.[59] Ideality factor describes how far the diode slope differs from an ideal diode slope.

However, it has already been known that high values of the ideality factors arise from a number of discrepancies in the device architecture involving the energetics and interfacial mismatches. Effects of nonuniform distribution of interface states, barrier inhomogeneities, tunnelling, bulk defects *etc.* Non ohmic behaviour of the electrodes also contributes to this. Employing suitable electron/hole transport and blocking buffer interface layers is necessary to overcome these bad effects. In this particular case of the gel Schottky diodes presented here the device structure used is only elementary without any interfacial buffer layers as the main objective of this part of the work is to peep into the potential of these gels to be used in microelectronic device applications. In this context, the conductivity, mobility and switching ratio values obtained here clearly point to the high potential of these two gels in such microelectronic applications. Comparing these two gels, conductivity values differ discernibly by about one order indicating a superior semiconducting nature for Eu–TA metallogel. Further, with the same device architecture and the limitations thereupon, Eu–TA diode exhibits much better switching, on–off ratio and lesser series resistance. As already mentioned the wide non-linear nature of the I–V characteristics also gives valuable information to this effect. It has been shown that one of the probable reason for the wide non linearity in the I–

Table 1 Semiconducting device parameters of Tb–TA and Eu–TA metallogels extracted from the electrical characteristics of the Schottky diodes fabricated with them as the active layers

Device	On/off ratio	Conductivity (S m^{-1})	Ideality factor	Barrier height (eV)	Series resistance (R_s) (kohm)		Electron mobility (cm^2 V^{-1} s^{-1})
					$\frac{dV}{d\ln I}$ *vs.* I	H *vs.* I	
Tb–TA	4316	1.45	15	0.63	2.78	2.79	1.6×10^{-4}
Eu–TA	784	0.14	16	0.606	3.98	3.82	1.3×10^{-4}

V characteristics. The *I–V* characteristics of both the gels (Fig. 10) show wide nonlinear nature and this wideness is more for Tb–TA compared to Eu–TA, and this can be traced to the higher series resistance value of the Tb–TA than that of the Eu–TA (Table 1).

4. Conclusions

To conclude, our study successfully synthesized two innovative metallogels incorporating Tb(III)- and Eu(III)-ions. This was achieved through rapid combination of respective acetate salts with benzene-1,3,5-tricarboxylic acid in DMF at room temperature. The self-assembly of these metallogel networks was driven by coordinated and cooperative interactions between the metal ions and the tartaric acid ligand. The mechanical stability of the synthesized metallogels was rigorously evaluated using rheological analysis. Microstructural examination through FESEM imaging revealed distinct architectures – a hierarchical flake-like structure for Tb(III)-metallogel and a rod-like structure for Eu(III)-metallogel. Detailed spectroscopic analysis, encompassing XRD, FTIR, and Raman measurements, shed light on the metallogels and their constituents. Notably, the Tb–TA metallogel exhibited a superior crystalline structure in comparison to the Eu–TA metallogel. FTIR spectra highlighted the presence of both coordinated and crystal water molecules in the gel compositions. Raman analysis further differentiated the two metallogels, showcasing the presence of a hetero-aromatic organic molecule exclusively in Tb–TA. Thermal behavior, as indicated by thermogravimetric analysis, revealed distinct degradation patterns for Tb–TA and Eu–TA metallogels, with the former displaying greater thermal stability, likely attributed to unique characteristics of their respective acetate combinations. Electrical and electronic property assessments demonstrated significant semiconducting characteristics for both metallogels, with Tb–TA metallogel exhibiting notably higher electrical conductivity. These findings underscore the potential utility of both metallogels in microelectronics applications. In summary, our work offers a comprehensive exploration of these novel Tb(III)- and Eu(III)-metallogels, revealing their distinct properties and potential for diverse device applications, particularly in the realm of microelectronics.

Conflicts of interest

The authors declare no competing financial interests.

Acknowledgements

S. D. is grateful to the UGC, New Delhi, for awarding him Dr DS Kothari Postdoctoral Fellowship (award letter number: no. F.4-2/2006(BSR)/CH/19-20/0224). S. B. thankfully acknowledges DST Inspire Faculty Research Grant (faculty registration no. IFA18-CH304; DST/INSPIRE/04/2018/000329).

Notes and references

1 N. M. Sangeetha and U. Maitra, *Chem. Soc. Rev.*, 2005, **34**, 821–836.
2 C. Richard, F. Balavoine, P. Schultz, T. W. Ebbesen and C. Mioskowski, *Science*, 2003, **300**, 775–778.
3 P. Dastidar, *Chem. Soc. Rev.*, 2008, **37**, 2699–2715.
4 (*a*) S. Dhibar, D. Ghosh, S. Majumdar and B. Dey, *ACS Omega*, 2020, **5**, 2680–2689; (*b*) S. Dhibar, A. Dey, R. Jana, A. Chatterjee, G. K. Das, P. P. Ray and B. Dey, *Dalton Trans.*, 2019, **48**, 17388–17394; (*c*) S. Dhibar, R. Jana, P. P. Ray and B. Dey, *J. Mol. Liq.*, 2019, **289**, 111–126; (*d*) S. Dhibar, A. Dey, D. Ghosh, A. Mandal and B. Dey, *J. Mol. Liq.*, 2019, **276**, 184–193; (*e*) S. Dhibar, A. Dey, A. Dey, S. Majumdar, A. Mandal, P. P. Ray and B. Dey, *New J. Chem.*, 2019, **43**, 15691–15699; (*f*) D. Ghosh, S. Dhibar, A. Dey, S. Mukherjee, N. Joardar, S. P. S. Babu and B. Dey, *J. Mol. Liq.*, 2019, **280**, 1–12; (*g*) S. Majumdar, T. Singha, S. Dhibar, A. Mandal, P. K. Datta and B. Dey, *ACS Appl. Electron. Mater.*, 2020, **2**, 3678–3685; (*h*) S. Majumdar, A. Dey, R. Sahu, S. Dhibar, P. P. Ray and B. Dey, *ACS Appl. Nano Mater.*, 2020, **3**, 11025–11036.
5 (*a*) C. Po, Z. Ke, A. Y. Y. Tam, H. F. Chow and V. W. W. Yam, *Chem.–Eur. J.*, 2013, **19**, 15735–15744; (*b*) S. Ganta and D. K. Chand, *Inorg. Chem.*, 2018, **57**, 3634–3645; (*c*) P. Chen, Q. Li, S. Grindy and N. Holten-Andersen, *J. Am. Chem. Soc.*, 2015, **137**, 11590–11593.
6 (*a*) Q. Lin, Q.-P. Yang, B. Sun, Y.-P. Fu, X. Zhu, T.-B. Wei and Y.-M. Zhang, *Soft Matter*, 2014, **10**, 8427–8432; (*b*) A. M. Amacher, J. Puigmartí-Luis, Y. Geng, V. Lebedev, V. Laukhin, K. Kramer, J. Hauser, D. B. Amabilino, S. Decurtins and S.-X. Decurtins, *Chem. Commun.*, 2015, **51**, 15063–15066; (*c*) S. Sarkar, S. Dutta, P. Bairi and T. Pal, *Langmuir*, 2014, **30**, 7833–7841.
7 (*a*) C. K. Karan and M. Bhattacharjee, *ACS Appl. Mater. Interfaces*, 2016, **8**, 5526–5535; (*b*) S. Dey, D. Datta, K. Chakraborty, S. Nandi, A. Anoop and T. Pathak, *RSC Adv.*, 2013, **3**, 9163–9166; (*c*) M.-O. M. Piepenbrock, N. Clarke and J. W. Steed, *Soft Matter*, 2010, **6**, 3541–3547; (*d*) M.-O. M. Piepenbrock, N. Clarke and J. W. Steed, *Langmuir*, 2009, **25**, 8451–8456.
8 (*a*) Z. Yao, Z. Wang, Y. Yu, C. Zeng and K. Cao, *Polymer*, 2017, **119**, 98–106; (*b*) P. Rajamalli, P. Malakar, S. Atta and E. Prasad, *Chem. Commun.*, 2014, **50**, 11023–11025.
9 K. Mitsumoto, J. M. Cameron, R.-J. Wei, H. Nishikawa, T. Shiga, M. Nihei, G. N. Newton and H. Oshio, *Chem.–Eur. J.*, 2017, **23**, 1502–1506.
10 X.-Q. Wang, W. Wang, G.-Q. Yin, Y.-X. Wang, C.-W. Zhang, J.-M. Shi, Y. Yu and H.-B. Yang, *Chem. Commun.*, 2015, **51**, 16813–16816.
11 B. Jiang, L.-J. Chen, G.-Q. Yin, Y.-X. Wang, W. Zheng, L. Xu and H.-B. Yang, *Chem. Commun.*, 2017, **53**, 172–175.
12 (*a*) F. Gou, J. Cheng, X. Zhang, G. Shen, X. Zhou and H. Xiang, *Eur. J. Inorg. Chem.*, 2016, 4862–4866; (*b*) N. Kelly, K. Gloe, T. Doert, F. Hennersdorf, A. Heine, J. Marz, U. Schwarzenbolz, J. J. Weigand and K. J. Gloe, *Organomet. Chem.*, 2016, **821**, 182–191.
13 (*a*) S. Dhibar, A. Dey, S. Majumdar, D. Ghosh, A. Mandal, P. P. Ray and B. Dey, *Dalton Trans.*, 2018, **47**, 17412–17420; (*b*) S. Dhibar, A. Dey, D. Ghosh, S. Majumdar, A. Dey, P. Mukherjee, A. Mandal, P. P. Ray and B. Dey,

ChemistrySelect, 2019, **4**, 1535–1541; (*c*) S. Dhibar, A. Dey, S. Majumdar, A. Dey, P. P. Ray and B. Dey, *Ind. Eng. Chem. Res.*, 2020, **59**, 5466–5473; (*d*) S. Dhibar, A. Dey, S. Majumdar, P. P. Ray and B. Dey, *Int. J. Energy Res.*, 2021, **45**, 5486–5499; (*e*) S. Dhibar, S. K. Ojha, A. Mohan, S. P. C. Prabhakaran, S. Bhattacharjee, K. Karmakar, P. Karmakar, P. Predeep, A. K. Ojha and B. Saha, *New J. Chem.*, 2022, **46**, 17189–17200; (*f*) S. Dhibar, H. Dahiya, K. Karmakar, S. Kundu, S. Bhattacharjee, G. C. Nayak, P. Karmakar, G. D Sharma and B. Saha, *J. Mol. Liq.*, 2023, **370**, 121020; (*g*) S. Dhibar, A. Dey, A. Dalal, S. Bhattacharjee, R. Sahu, R. Sahoo, A. Mondal, S. M. Rahaman, S. Kundu and B. Saha, *J. Mol. Liq.*, 2023, **370**, 121021; (*h*) S. Dhibar, S. Babu, A. Mohan, G. K. Chandra, S. Bhattacharjee, K. Karmakar, P. Karmakar, S. M. Rahaman, P. Predeep and B. Saha, *J. Mol. Liq.*, 2023, **375**, 121348; (*i*) K. Karmakar, A. Dey, S. Dhibar, R. Sahu, S. Bhattacharjee, P. Karmakar, P. Chatterjee, A. Mondal and B. Saha, *RSC Adv.*, 2023, **13**, 2561–2569; (*j*) S. Dhibar, B. Pal, K. Karmakar, S. Kundu, S. Bhattacharjee, R. Sahoo, S. M. Rahaman, D. Dey, P. P. Ray and B. Saha, *ChemistrySelect*, 2023, **8**, e202204214.

14 (*a*) Z. Yao, Z. Wang, Y. Yu, C. Zeng and K. Cao, *Polymer*, 2017, **119**, 98–106; (*b*) P. Rajamalli, P. Malakar, S. Atta and E. Prasad, *Chem. Commun.*, 2014, **50**, 11023–11025.

15 (*a*) S. Ganta and D. K. Chand, *Dalton Trans.*, 2015, **44**, 15181–15188; (*b*) L. Yang, L. Luo, S. Zhang, X. Su, J. Lan, C.-T. Chen and J. You, *Chem. Commun.*, 2010, **46**, 3938–3940; (*c*) B. Xing, M.-F. Choi, Z. Zhou and B. Xu, *Langmuir*, 2002, **18**, 9654–9658; (*d*) X. Ma, S. Liu, Z. Zhang, Y. Niu and J. Wu, *Soft Matter*, 2017, **13**, 8882–8885.

16 C. A. Offiler, C. D. Jones and J. W. Steed, *Chem. Commun.*, 2017, **53**, 2024–2027.

17 S. Dhibar, A. Dey, S. Majumdar, D. Ghosh, P. P. Ray and B. Dey, *ACS Appl. Electron. Mater.*, 2019, **1**, 1899–1908.

18 R. G. Weiss and P. Terech, *Molecular Gels: Materials with Self-Assembled Fibrillar Networks*, Springer, Dordrecht, 2005.

19 (*a*) T.-A. Asoh and A. Kikuchi, *Chem. Commun.*, 2012, **48**, 10019–10021; (*b*) X. Wang, F. Liu, X. Zheng and J. Sun, *Angew. Chem., Int. Ed.*, 2011, **50**, 11378–11381; (*c*) H. Wang, M. B. Hansen, D. W. P. M. Löwik, J. C. M. van Hest, Y. Li, J. A. Jansen and S. C. G. Leeuwenburgh, *Adv. Mater.*, 2011, **23**, H119–H124.

20 (*a*) A. Y.-Y. Tam and V. W.-W. Yam, *Chem. Soc. Rev.*, 2013, **42**, 1540–1567; (*b*) C. Tomasini and N. Castellucci, *Chem. Soc. Rev.*, 2013, **42**, 156–172; (*c*) L. Meazza, J. A. Foster, K. Fucke, P. Metrangolo, G. Resnati and J. W. Steed, *Nat. Chem.*, 2013, **5**, 42–47.

21 (*a*) M. Shirakawa, N. Fujita and S. Shinkai, *J. Am. Chem. Soc.*, 2003, **125**, 9902–9903; (*b*) J. R. Moffat, G. J. Seeley, J. T. Carter, A. Burgess and D. K. Smith, *Chem. Commun.*, 2008, 4601–4603.

22 (*a*) Y. Xu, Q. Wu, Y. Sun, H. Bai and G. Shi, *ACS Nano*, 2010, **4**, 7358–7362; (*b*) S. Burattini, B. W. Greenland, D. H. Merino, W. Weng, J. Seppala, H. M. Colquhoun, W. Hayes, M. E. Mackay, I. W. HamLey and S. J. Rowan, *J. Am. Chem. Soc.*, 2010, **132**, 12051–12058.

23 A. R. Hirst, B. Escuder, J. F. Miravet and D. K. Smith, *Angew. Chem., Int. Ed.*, 2008, **47**, 8002–8018.

24 (*a*) X. Ji, Y. Yao, J. Li, X. Yan and F. Huang, *J. Am. Chem. Soc.*, 2013, **135**, 74–77; (*b*) M. Ikeda, R. Ochi and I. Hamachi, *Lab Chip*, 2010, **10**, 3325–3334.

25 E. Ye, P. L. Chee, A. Prasad, X. Fang, C. Owh, V. J. J. Yeo and X. J. Loh, *Mater. Today*, 2014, **17**, 194–202.

26 S. M. Mehta, T. Jin, I. Stanciulescu and K. J. Grande-Allen, *Acta Biomater.*, 2018, **75**, 52–62.

27 X. Cheng, J. Pan, Y. Zhao, M. Liao and H. Peng, *Adv. Energy Mater.*, 2018, **8**, 1702184–1702199.

28 X.-Q. Dou and C.-L. Feng, *Adv. Mater.*, 2017, 1604062–1604082.

29 J. Wang, Z. Wang, J. Gao, L. Wang, Z. Yang, D. Kong and Z. Yang, *J. Mater. Chem.*, 2009, **19**, 7892–7896.

30 N. Shi, G. Yin, M. Han and Z. Xu, *Colloids Surf., B*, 2008, **66**, 84–89.

31 X. Jia and K. L. Kiick, *Macromol. Biosci.*, 2009, **9**, 140–156.

32 D. Marsh, *Biochemistry*, 1980, **19**, 1632–1637.

33 B. O. Okesola and D. K. Smith, *Chem. Soc. Rev.*, 2016, **45**, 4226–4251.

34 W.-L. Guan, K. M. Adam, M. Qiu, Y.-M. Zhang, H. Yao, T.-B. Wei and Q. Lin, *Supramol. Chem.*, 2020, **32**, 578–596.

35 W. H. Binder, L. Petraru, T. Roth, P. W. Groh, V. Pálfi, S. Keki and B. Ivan, *Adv. Funct. Mater.*, 2007, **17**, 1317–1326.

36 A. Khan, R. R. Kisannagar, C. Gouda, D. Gupta and H.-C. Lin, *J. Mater. Chem. A*, 2020, **8**, 19954–19964.

37 B. Xue, M. Qin, T. Wang, J. Wu, D. Luo, Q. Jiang, Y. Li, Y. Cao and W. Wang, *Adv. Funct. Mater.*, 2016, **26**, 9053–9062.

38 S. Biswas, U. Chatterjee, S. Sarkar, F. Khan, D. Bera, M. Mukhopadhyay, S. Goswami, S. Chakrabarti and S. Das, *Colloids Surf., B*, 2020, **188**, 110803.

39 P. Chen, Q. Li, S. Grindy and N. H. Andersen, *J. Am. Chem. Soc.*, 2015, **137**, 11590–11593.

40 H. Su, S. Zhu, M. Qu, R. Liu, G. Song and H. Zhu, *J. Phys. Chem. C*, 2019, **123**, 15685–15692.

41 N. Dey, S. K. Samanta and S. Bhattacharya, *ACS Appl. Mater. Interfaces*, 2013, **5**, 8394–8400.

42 D. Rambabu, P. Negi, A. Dhir, A. Gupta and Pooja, *Inorg. Chem. Commun.*, 2018, **93**, 6–9.

43 A. Biswas, S. Mukhopadhyay, R. S. Singh, A. Kumar, N. K. Rana, B. Koch and D. S. Pandey, *ACS Omega*, 2018, **3**, 5417–5425.

44 Q. Lin, T.-T. Lu, X. Zhu, B. Sun, Q.-P. Yang, T.-B. Wei and Y.-M. Zhang, *Chem. Commun.*, 2015, **51**, 1635–1638.

45 G. S. Thool, K. Narayanaswamy, A. Venkateswararao, S. Naqvi, V. Gupta, S. Chand, V. Vivekananthan, R. R. Koner, V. Krishnan and S. P. Singh, *Langmuir*, 2016, **32**, 4346–4351.

46 T. Zhang and W. Lin, *Chem. Soc. Rev.*, 2014, **43**, 5982–5993.

47 (*a*) H. Li, J. Guo, J. Ren, Y. Li and X. Yu, *J. Mater. Chem. A*, 2022, **10**, 7941–7947; (*b*) W. Hou, X. Yu, Y. Li, Y. Wei and J. Ren, *ACS Appl. Mater. Interfaces*, 2022, **14**, 57387–57398; (*c*) L. Cao, P. Wang, X. Miao, H. Duan, H. Wang, Y. Dong, R. Ma, B. Zhang, B. Wu, X. Li and P. J. Stang, *Inorg. Chem.*, 2019, **58**, 6268–6275.

48 (*a*) K. Singh, P. Pradhan, S. Priya, S. Mund and S. Vaidyanathan, *Dalton Trans.*, 2023, **52**, 13027–13057; (*b*) K. Awaya, K. Iso and S. Ida, *Nanoscale*, 2022, **14**, 16874–16882; (*c*) S. Sedghiniya, J. Soleimannejad, M. Foroutan, M. Ebrahimi and V. F. Naeini, *RSC Adv.*, 2021, **11**, 36801–36813.
49 Q. Zhu, L. Zhang, K. V. Vliet, A. Miserez and N. Holten-Andersen, *ACS Appl. Mater. Interfaces*, 2018, **10**, 10409–10418.
50 F. F. da Silva, F. L. de Menezes, L. L. da Luz and S. Alves Jr, *New J. Chem.*, 2014, **38**, 893–896.
51 S. Bhowmik, S. Banerjee and U. Maitra, *Chem. Commun.*, 2010, **46**, 8642–8644.
52 J. Zhang, N. Gerile, J. Davaasambuu, A. Bolag, E. Hua and Y. Zhang, *Arab. J. Chem.*, 2021, **14**, 103033.
53 B. A. A. Balboul and M. I. Zaki, *J. Anal. Appl. Pyrolysis*, 2011, **92**, 137–142.
54 S. A. Soliman and B. M. Abu-Zied, *Thermochim. Acta*, 2009, **491**, 84–91.
55 C. Tao, X. Yuan, Q. Yin, H. Yan, W. Ni, L. Yan and L. Zhang, *J. Mater. Sci.: Mater. Electron.*, 2016, **27**, 5715–5722.
56 C. Hernández-Fuentes, R. Ruiz-Guerrero, A. d. J. Morales-Ramírez, P. Molina-Maldonado and D. Y. Medina-Velazquez, *Crystals*, 2020, **10**, 674.
57 P. Xiao, J. J. Zhang, Z. Q. Wang and H. Lin, *Adv. Mater. Sci. Eng.*, 2016, **2016**, 1–11.
58 G. Mahalakshmi and V. Balachandran, *Spectrochim. Acta, Part A*, 2014, **124**, 535–547.
59 K. Sel, S. Demirci, E. Meydan, S. Yildiz, O. F. Ozturk, H. Al-Lohedan and N. Sahiner, *J. Electron. Mater.*, 2015, **44**, 136–143.
60 S. K. Cheung and N. W. Cheung, *Appl. Phys. Lett.*, 1986, **49**, 85–87.
61 A. Dey, S. Middya, R. Jana, M. Das, J. Datta, A. Layek and P. P. Ray, *J. Mater. Sci. Mater. Electron.*, 2016, **27**, 6325–6335.
62 K. Ghosh, S. Sil, P. P. Ray, J. Ortega-Castro, A. Frontera and S. Chattopadhyay, *RSC Adv.*, 2019, **9**, 34710–34719.
63 P. N. Murgatroyd, *J. Phys. D: Appl. Phys.*, 1970, **3**, 151–156.
64 A. Hajibadali, M. B. Nejad and G. Farzi, *Braz. J. Phys.*, 2015, **45**, 394–398.